Sensors & Diagnostics

PAPER

View Article Online
View Journal | View Issue

Cite this: *Sens. Diagn.*, 2023, **2**, 714

Nano-dimensionality effect on electrochemical aptamer-based sensor performance for MUC1 liquid biopsy

Ashkan Koushanpour,[a] Edward J. Harvey[a] and Geraldine E. Merle *[ab]

The modularity of electrochemical aptamer-based (E-AB) sensors has made them useful candidates for real-time and specific determination of molecular targets (irrespective of their chemical reactivity). In this work, we have emphasized the role of the electrode surface's morphological dimensions on the E-AB sensor's performance for the detection of breast cancer biomarker MUC1 in the human serum sample. To accomplish this, bottom-up approaches were utilized for the synthesis of one- and three-dimensional gold substrates (with 0.072 cm^2 and 0.079 cm^2 ECSAs, respectively) that were later used in the construction of E-AB sensors, and the results were compared to a planar gold electrode (two-dimensional with an ECSA of 0.02 cm^2). The selection of a regular gold electrode as the two-dimensional substrate was essential to make the study relevant and comparable with the widely used type of electrode that is commonly used in the fabrication of E-AB sensors. Our data show that the E-AB sensor based on the three-dimensional gold substrate with a limit of detection (LOD) of 6.8 nM did not significantly improve the regular electrode (two-dimensional) with a LOD of 7.8 nM, whereas the one-dimensional gold substrate proved to be the most electrochemically sensitive surface with a LOD of 3.5 nM. This enhancement is likely due to the attributes of the surface organization. Therefore, our findings suggest that a large surface area alone does not necessarily guarantee a better sensitivity unless causing a fruitful contribution to the aptamers' surface organization.

Received 18th January 2023,
Accepted 23rd March 2023

DOI: 10.1039/d3sd00021d

rsc.li/sensors

1. Introduction

Aptamers have attracted much attention in diagnostic medicine due to their easy synthesis protocols, low cost, great stability, and ability to recognize and bind a broad range of target analytes.[1–3] These short, single-stranded DNA or RNA molecules have been endorsed as recognition elements in biosensors, particularly in electrochemical aptamer-based (E-AB) sensors.[4] E-AB sensors are comprised of a surface-bound redox-modified probe aptamer (stem-loop) that is immobilized on the surface of a gold electrode *via* self-assembled monolayer (SAM) chemistry. In the absence of a target, the redox entity is found at the proximity of the electrode where a large current flows. After target addition, the hybridization-induced secondary-structure change will position the redox moiety away from the surface decreasing the current. This change in the current is readily measurable and is relatable to the target concentration.

The characteristics of an interfacial region are key to the performance of E-AB sensors.[5–7] Generally the SAM of the oligonucleotides on the electrode surface is considered the most well-defined building block in the construction of an E-AB sensor and therefore has been tremendously employed to immobilize different probes on an Au surface.[8] In addition, the goal in the optimization of an E-AB sensor is to find a condition that affords the largest conformational changes[9] of aptamers, as well as the optimum strand-to-strand interspace.[10,11] As the interfacial recognition layer develops, several properties have been shown to be impactful such as aptamer organization/orientation,[12–14] aptamer length,[15] chemistry,[16] spatial location of the electrochemical tag,[17] surface density, and backfilling strategies.[18,19] The incorporation of nanostructures can significantly contribute to the progress of many of these features.[20] For example, nanostructures can stabilize the DNA or RNA strands,[21] enhance the sensitivity,[22] and enable a rapid electron transfer.[23] Nanomaterials possess many unique physical and chemical properties emerging from their nanosize (*e.g.*, varying in electrical conductivity and optical characteristics compared to their bulk alternatives).[24,25] Interestingly, these attributes can be tailored and optimized for specific applications by manipulation of their properties including size, surface area, dimensionality, and porosity.[26] There are many reports showing the influence of the size and shape of nanostructures on the SAM quality, target binding, and surface chemistry.[27–29]

[a] *Department of Surgery, Faculty of Medicine, McGill University, Montreal, Canada*
[b] *Department of Chemical Engineering, Polytechnique Montreal, Montreal, Canada. E-mail: geraldine.merle@polymtl.ca*

Among metal nanostructures, gold is the most widely used[30] due to its ease of synthesis, biocompatibility, excellent conductive properties, and strong electron carriers. Given that they tend to display size, shape, and composition-dependent properties,[31] such as morphologies (*e.g.*, shape and surface structure), and distance-dependent properties (*e.g.*, plasmonic and quantum confinement effect), Au nanomaterials have been studied and applied to biomedical applications.[32–34] Recently, surface nano-effects have received considerable attention for the fabrication of E-AB sensors as they provide superior analytical performance, because they not only can significantly increase the loading amount of DNA probes and protect the aptamers from degradation and denaturation, thus improving their stability and shelf-life but also may serve as a medium to enhance the electrochemical response in a hybridization reaction.[35–37] The effect of dimensionality on the electrochemically active surface area, includes the specific morphology of the nanostructures, as well as the porosity. For example, 3D nanostructures can be either 3D spatial ensembles of 1D and/or 2D nanostructures or 3D nanoporous structures and 3D hierarchical nanostructured materials. Given the large array of materials and microscopic surface features, it is unlikely that different 3D nanostructured electrodes will produce similar results and performances. Plaxco *et al.* have shown the application of two different techniques to produce 3D nanoporous Au for the miniaturization of an *in vivo* E-AB sensor to detect vancomycin.[38] Despite both exhibiting a 3D nanostructure, one approach generated a 100-fold increase compared to a 2–3-fold increase for the second technique. This study demonstrated that the way that the 3D nanostructures are fabricated is as important as their dimensionality for the immobilization of aptamers. Indeed, as it was demonstrated by Plaxco.[38] *et al.* that the fabrication process could affect the surface chemistry and morphology of the nanostructures, which could influence the binding affinity and specificity of the immobilized aptamers. Additionally, the fabrication process can introduce defects, impurities, or roughness on the surface of the nanostructures, which can compromise the stability and sensitivity of the biosensor. Other works have shown that these nanomaterials were key to enabling a precise long-term measurement of a specific molecular target *in vivo*.[39] In addition, Kelley *et al.* have demonstrated that utilization of nanostructured gold surface dramatically enhances the hybridization efficiency by more than 30% compared to the same probe molecules when tethered to a smoother surface (<5%).[40] Moreover, Shahrokhian and his co-workers[41] developed a label-free aptasensor based on nanoporous gold for the detection of salmonella by selective removal of the Cu from Au–Cu alloy. They have observed that the nanoporous gold morphology is more efficient in the formation of SAM in comparison with a planar gold electrode.

So far, there have been very few attempts at addressing the impact of the dimensionality of gold nanostructures on the E-AB sensor's analytical performance. In this study, we aim to identify the impact of the gold substrate nano-dimensionality on the performance of the E-AB biosensor. As depicted in Fig. 1, three different Au surfaces were engineered to immobilise MUC1 aptamers for the detection of MUC1 in the peripheral blood of cancer patients.

To do so, bottom-up approaches were employed to synthesise one-dimensional (1D) and three-dimensional (3D) gold substrates, which later serve as substrates for the aptamer functionalization. The fabricated E-AB biosensors were then employed in the detection of the breast cancer biomarker MUC1 in human serum samples and ultimately compared with a regular gold electrode (2D) as the benchmark of the comparison.

2. Experimental

2.1. Reagents

Reagents acquired from Sigma-Aldrich were used as received unless otherwise stated: potassium hexacyanoferrate(II) trihydrate $K_4Fe(CN)_6$, human male AB plasma, USA origin, sterile-filtered, 6-mercapto-1-hexanol (C6-OH), and tris-(2-carboxyethyl) phosphine hydrochloride (TCEP). HPLC-purified and desalted anti-MUC1 DNA aptamers, HO-$(CH_2)_6$-SS-$(CH_2)_6$-O-5′-GCA GTT GAT CCT TTG GAT ACC CTG-G-3′-(CH_2)7-NHCO-$(CH_2)_3$-methylene blue (MB), referred to as MB-anti-MUC1 aptamer, were used.

The products were purchased from Biosearch Technologies Inc. (Novato, CA). The sequence was reported by Ferreira *et al.* as S1.3/S2.2.[42]

The 60 mer 3× VTR MUC1 peptide (PDT RPA PGS TAP PAH GVT SAP DTR PAP GST APP AHG VTS APD TRP APG STA PPA HGV TSA) was purchased from PL Laboratories Inc. (Vancouver, Canada). The peptides were suspended in a phosphate buffer (137 mM NaCl, 10 mM Na_2HPO4, 1.4 mM KH_2PO_4, 2.7 mM KCl, pH 7.2) and stored at −20 °C.

2.2. Preparation of E-AB sensors

E-AB sensors (2D) were fabricated using a 1.6 mm diameter gold disk electrode (BAS, West Lafayette, IN). The electrode was polished with Buehler alumina slurry (1 and 0.05 μm) for 5 min, sonicated for 2 min and then transferred to a "piranha" solution (3 : 1 ratio of H_2SO_4 : H_2O_2) for 5 min. Finally, 25 cyclic voltammetry scans were conducted in 0.1 M H_2SO_4 solution from 1.4 V to 0.1 V before the electrode was incubated in 100% ethanol for another 5 min. To fabricate the E-AB sensors, the relevant aptamer solution was diluted to 0.07 μM (see below). The gold electrode was incubated in

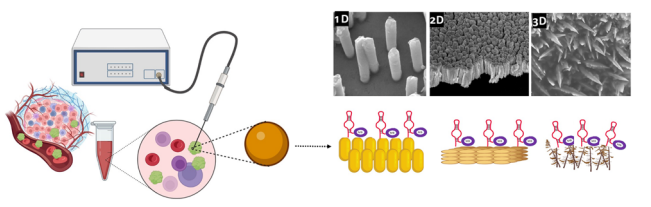

Fig. 1 Schematic illustration of three different gold surface dimensionalities to detect MUC1, a useful prognostic biomarker for predicting cancer outcomes.

the aptamer solution for 2 h. The electrode surface was then incubated in 2 mM mercaptohexanol (MCH) for 2 h to block non-specifically adsorbed aptamers. The surface probe density (Γ) of each electrode was estimated by measuring the area under the reduction peak in cyclic voltammogram at 200 mV s^{-1} in 10 mM phosphate buffer saline solution (PBS) (containing 2.92 g of NaCl, 0.0690 g of NaH_2PO_4, and 0.071 g of Na_2HPO_4 plus 50 μL of 1 M $MgCl_2$ in 25 mL of deionized water, Millipore, nanopure water, 17.5 MΩ cm^{-1}), pH 7.2 (eqn (1)).

$$\Gamma = \frac{Q}{(nFA)} \quad (1)$$

where Q is the area of the reduction peak, n is the number of electrons per redox event (n = 2 for MB), F is Faraday's constant, and A is the area of the gold electrode, which is 0.020 cm^2. Accordingly, the probe density was obtained to be 4.7×10^{12} molecules per cm^2. The same fabrication protocol was followed for the preparation of other E-AB sensors featuring 1D and 3D gold nanostructures.

Electrochemical optimizations were performed in 10 mM PBS using square wave voltammetry (SWV) with an amplitude of 50 mV, a step potential of 5 mV and a frequency of 20 Hz. Electrochemical interrogations were recorded from 0.1 V to −0.5 V *versus* Ag/AgCl (sat. KCl) reference electrode. All other electrochemical procedures were performed in 50% diluted human serum. This 1 : 2 dilution was chosen not only to decrease the concentration of interfering substances that may interfere with the electrochemical measurements but also to increase the ionic conductivity allowing for better ion movement and more accurate measurements. The latter proved to display an identical signalling current to that of the PBS buffer solution.

2.3. Synthesis of gold nanostructures

2.3.1. Gold nanospike (NS) synthesis. A gold NS surface was prepared *via* a shape-controlled electrochemical method.[43] Briefly, gold NSs were electrochemically formed on a gold disk electrode from a solution containing 6.9 mM $HAuCl_4$ and 0.5 mM $Pb(CH_3COO)_2$. Electrochemical deposition was performed for 600 s at 0.05 V using Ag/AgCl (sat. KCl) as a reference electrode and a graphite as an auxiliary electrode.

2.3.2. Gold nanorod (NR) synthesis. The soft template-assisted electrodeposition method was used to produce gold NR in a track-etched polycarbonate (TEPC) membrane (pore diameter of 200 nm). To achieve this, a 100 nm thick gold layer was prepared using a sputtering method on the TEPC membrane that served as a conductive substrate. Next, we assembled the TEPC membrane on carbon with 2% Nafion acetate solution as polyelectrolyte glue (Fig. 2). This unit was then placed in a mixture of 5.8 mM $HAuCl_4$ and 0.1 M $HClO_4$ for 2 h. Then gold was electrodeposited at a constant potential of 0.18 V for 110 s. The membrane was finally dissolved in dichloromethane for 5 min.

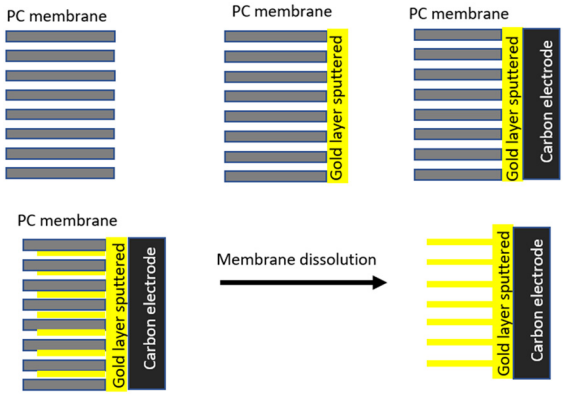

Fig. 2 Schematic representation of template-based synthesis of gold NRs using TEPC.

2.4. Physico-chemical characterization and electrochemical measurements

The surface morphology was investigated by FEI Quanta 450 environmental field-emission scanning electron microscopy (FE-ESEM), and energy-dispersive X-ray spectroscopy (EDX) was used to determine the chemical composition of the 3D gold substrate surface. Electrochemical measurements were performed using a potentiostat/galvanostat (VersaSTAT 4, Princeton Applied Research) with a three-electrode system consisting of an Ag/AgCl (sat. KCl) reference electrode, a Pt wire counter electrode, and a gold disk electrode. Electrochemical measurements were performed in 50% diluted human serum samples using SWV as described in section 2.2.

Results and discussion

In this study, we investigated the influence of the gold surface dimensionality on the E-AB sensor's analytical performance in a signal-off sensor directed against the protein MUC1 in diluted human serum samples. Each sensor includes a DNA aptamer (25 nucleotides) that has been attached to the gold surface at its 5′-terminus *via* gold–thiol chemistry and a redox-active marker (MB) at the 3′-terminus. The E-AB sensors were built by immobilizing these modified aptamers through gold-alkanethiol chemistry on three different nanostructured gold surfaces: control 2D, 3D NS, and 1D NR. Fig. 3A–C show the scanning electron micrographs of the top view of a representative TEPC membrane (A) and the corresponding Au NR electrode after the removal of the TEPC membrane (B and C).

The electrode surface is fully covered by high-density (~5.0×10^8 NR cm^{-2}) and parallel NRs of 200 nm in diameter and 800 nm in length, with an inter-distance of 300 nm to 700 nm between them (Fig. 3B and C).

In Fig. 3D and E, the surface of the electrode exhibits a uniform coating of well-defined Au NSs with prismatic tapering ends. The top view of 3D gold NSs indicates a base thickness dimension of about ~350 nm (Fig. 3E and F) and approximately 500 nm in length. Lastly, in Fig. 3G one can

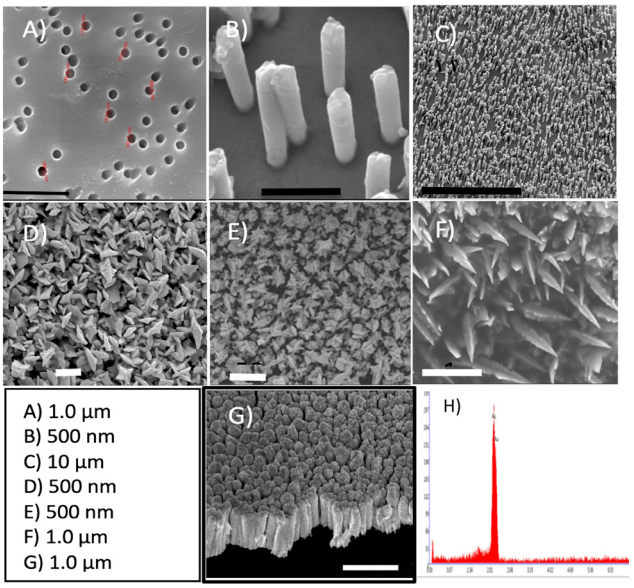

Fig. 3 Scanning electron micrographs of the gold substrates: A) surface of the TEPC membrane, B) close view of the 1D NR, C) the electrode surface with a 1D orientation, D) zoomed-in top-view of the 3D NS, E) zoomed-out top-view of the 3D NS, F) tilted view of the 3D NS, G) side-view of the 2D gold surface, and H) EDX spectrum from the 3D gold NS.

see the side-view of the 2D sputtered-gold surface. Complete removal of Pb for the NS structure has been confirmed with EDX analysis as shown in Fig. 3H. Fig. 4A shows the cyclic voltammograms obtained at each Au surface. The evolution of larger peaks (both oxidation and reduction) for NS and NR (black and blue curves) *vs.* 2D gold surface (red curve) account for the contribution of the higher surface area of the corresponding Au NS and Au NR nanostructures. Also, it is evident that, compared to the Au 2D electrode (red curve), the other two counterparts (black and blue curves) have shown 0.05 V reduction in the peak-to-peak separation ($\Delta E = E_{pa} - E_{pc}$). It has been demonstrated that the higher surface area and evolution of higher degree of edge effect are key factors to address these effects.[44,45]

The electrochemical active surface area (ECSA) of the Au control, Au NSs and Au NRs were determined using cyclic voltammetry in 0.1 M H_2SO_4 solution. The area under the reductive cathodic peak (background current excluded) on

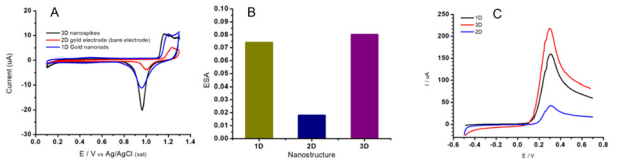

Fig. 4 A) CV curves of a gold electrode featuring various morphological aspects of 1D, 2D, and 3D nanostructures. Cyclic voltammetry was performed in 0.1 H_2SO_4 solution with a sweep rate of 0.05 V s^{-1}. B) The ECSA comparison. C) The corresponding LSV curves obtained in water solution containing $K_4Fe(CN)_6$ (10.0 mM), v = 0.1 V s^{-1}.

the voltammogram is proportional to the real surface area (ECSA = Q/390 uC cm^{-2}) and is therefore an indication of surface roughness.

ECSA was calculated from the cathodic peak which is related to the removal of the monolayer of oxide formed on the surfaces during the onward scan of cyclic voltammetry. As expected, the ECSA of the Au NSs (0.079 cm^2) and NRs (0.072 cm^2) revealed significant enhancement compared to that of the control Au electrode (0.02 cm^2), as shown in Fig. 4B. Fig. 4C demonstrates the effect of surface area enhancement on the corresponding electrochemical activity. Given the geometrical area of the Au 2D electrode *ca.*, 0.02 cm^2, roughness factors (R_f, the ratio of ECSA to geometrical area) of 3.95 and 3.6 were calculated for the NS and NR, respectively. This evidence, the apparent roughness value enhancement, will account for the successful preparation of gold nanostructures on the electrodes.

Given the E-AB sensor's signalling mechanism,[46] in which detection is achieved by relying on binding induced changes in the electron transfer rate between a surface-bound, reporter-modified aptamer and an electrode, the electron transfer rate before and after MUC1 hybridization at the electrode surface is dependent on the SWV frequency used to interrogate the electrode, as well as the packing density of the aptamers. The latter was optimized by measuring the signal response of MUC1 on the aptamer-modified gold electrode using various concentrations of the probe aptamer. An optimal probe density was achieved at 4.7×10^{12} molecule per cm^{-2}, corresponding to an aptamer solution of 70 nM. Due to the size of surface nanostructures (>60 nm),[47] a similar probe surface density of 4.7×10^{12} molecule per cm^{-2} is expected for 1D and 3D based E-AB sensors.[48] Given that they will share the same probe surface density, the difference in performance will be only the result of surface dimensionality.

Au nanostructures can influence the kinetics of hybridization by interfering with the target diffusion, target/probe interaction and aptamer conformational changes. Fig. 5 reveals whether micro- and macrostructural features of the three nanostructures will influence the sensitivity and thus the aptamer's performance. The kinetics of hybridization (response time) *vs.* gain for the three electrodes were monitored and compared. Here the response time is used as a measure for identifying the kinetics of hybridization.[49]

A steep hybridization curve demonstrates a better affinity and accessibility of the target to the probe. The results are displayed in Fig. 5, and their response time *vs.* signal gain (defined as the ratio of the current change at a given target concentration and the initial current) were compared. The results show that the electrodes exhibited a similar behaviour in terms of gain variations *vs.* time (hybridization kinetic) until a plateau is reached. The highest gain (~60%) was achieved for Au NR (1D) electrodes in 70 minutes whereas Au NS (3D) and Au control (2D) required 70 minutes to reach a gain of 40%. These gain variations, in the case of Au NR

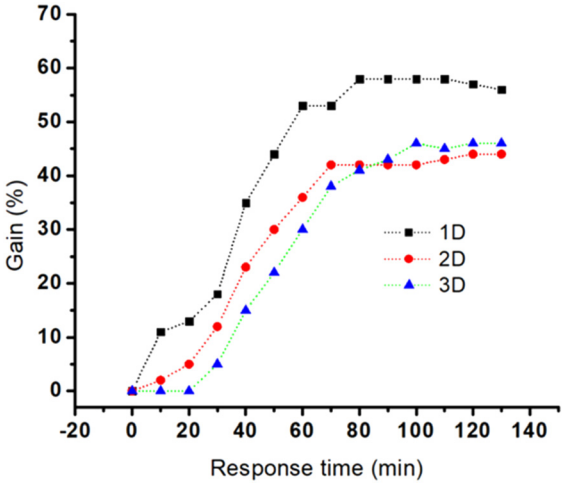

Fig. 5 Representation of the typical response time (signal suppression) of the various E-AB sensors featuring 1D, 2D, and 3D gold substrates during 2 h incubation with a saturated concentration of MUC1 in 50% diluted human serum. Data points have been collected from a single measurement.

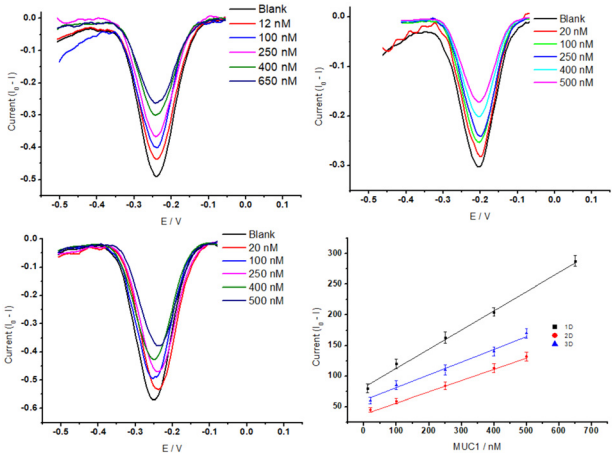

Fig. 6 SWV responses of the E-AB sensors featuring 1D (A), 2D (B), and 3D (C) gold substrates after incubating with MUC1 at different concentrations. (D) Collected calibration lines for the detection of MUC1 based on various dimensionalities. The experiment was carried out with an amplitude of 50 mV, a step of 5 mV, and a frequency of 20 Hz in the 50% diluted human serum samples.

(1D), started to be measurable only after 10 min in contact with MUC1, whereas Au Ns (3D) and the control electrodes (2D) needed at least 20–30 min. This hybridization kinetic behaviour is likely due to the difference between accumulation of MUC1 on the sensor surface and can be easily influenced by the surface geometry-induced steric hindrances.[50] The influence of Au dimensionalities on the analytical performance of the corresponding E-AB sensors was analysed with increased concentrations from 0 nM to 650 nM of MUC1 in the 50% diluted human serum samples. The corresponding signal changes (Δi is the change of peak current before and after addition of MUC1) were monitored *via* an SWV technique (Fig. 6A–C). The SWV voltammograms showed a proportional decrease of MB current at ~−0.25 V *vs.* Ag/AgCl with the increase of MUC1 concentrations.

The SWV data were converted into a calibration plot by plotting the signal suppression *vs.* concentration of MUC1 (Fig. 6D).

MB redox peak linearly decreased in response to the addition of MUC1 for the three electrodes. We obtained the corresponding regression equation of $\Delta i = (0.33 \pm 0.03)x + (81.51 \pm 9.9)$ ($R^2 = 99.47$, $N = 5$), $\Delta i = (0.18 \pm 0.03)x + (37.72 \pm 7.6)$ ($R^2 = 99.30$, $N = 5$), and $\Delta i = (0.20 \pm 0.03)x + (60.56 \pm 7.6)$ ($R^2 = 98.82$, $N = 5$), for NRs (1D), control (2D) and NSs (3D) featuring E-AB sensors (based on 95% confidence interval, $t_{(n-2)} = 3.18$).[51] A limit of detection (LOD) (calculated by LOD $= \frac{3S_b}{m}$, where S_b is the standard deviation of the blank measures and m is the slope of the calibration plot obtained from the linear regression analysis) of 3.5 nM, 7.8 nM, and 6.8 nM was correspondingly estimated for NRs (1D), 2D control, and NSs (3D) featuring E-AB sensors. The lowest Au dimension appears to provide the best sensitivity as well as, a wider LDR from 12 nM to 650 nM, compared to 3D NS and Au 2D electrodes that exhibit an LDR between 20 nM to 500 nM. The observed behaviour can be most likely explained through the influence of the surface morphology on the surface organization of aptamers. The large surface area of the 1D gold substrate (0.072 cm^2), compared to the gold 2D substrate (0.02 cm^2) significantly increased the immobilization sites for the MUC1 probe aptamers. Despite exhibiting a higher surface area, 3D Au NS did not perform as well as 1D Au NS. This discrepancy between the surface area and electrochemical performances can be caused by the orientation of aptamers which vary strongly with the surface chemistry and morphology of the substrate. It has been shown that gold nanorods have a more uniform surface morphology and surface charge distribution, which allows for better alignment and immobilization of the aptamers on the surface. In contrast, gold nanospikes and gold layers have more irregular surface features, such as sharp edges and rough surfaces, which can disrupt the alignment of the aptamers and result in less consistent orientation. Additionally, the binding affinity of the aptamer for the substrate can also play a role in the orientation of the aptamer. If the aptamer has a stronger affinity to one surface compared to another, it may be more likely to align properly on that surface. Therefore, while the exact reason on the effect of surface area on the signal gain, which is offset in the 3D structure, is not entirely clear, irregular surface features, sharp edges and weaker binding affinity are believed to lead to unproper alignment of aptamers on that surface, and additionally the nanospike morphology might also be unfavourable for the conformational change after target hybridization.

To investigate the repeatability, we prepared three fresh E-AB sensors and incubated them with saturated concentration of MUC1 in 50% human serum samples (Fig. 7).

All E-AB sensors exhibited similar signalling behaviours with relative standard deviations (RSD) of 4.1% (NR), 4.5% (control), and 3.7% (NS), respectively. These values

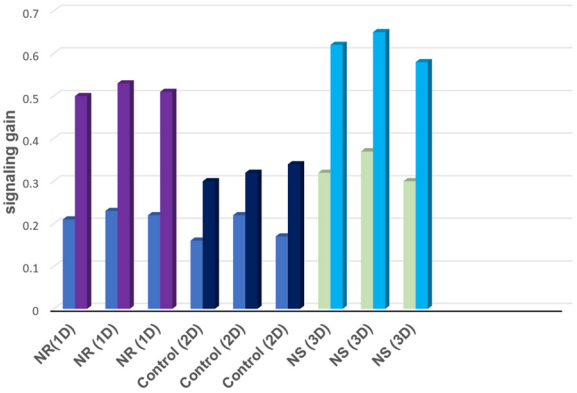

Fig. 7 Shows repeatability results for three freshly prepared E-AB sensors 1D, 2D, and 3D. The left bar represents the initial signal of the E-AB sensor, and the right bar is the signal gain after target hybridization.

demonstrate that the repeatability character of the E-AB sensors within the corresponding time frame (90 min) was satisfactory. Moreover, the stability of the fabricated E-AB sensors was also examined. Following the storage in the refrigerator at 4 °C for 9 days, NR (1D) and NS (3D) based aptasensors retained 91% and 95% of their initial currents, respectively, whereas the control electrode (2D) lost more than 90% of its initial value after only 3 days. The stabilization of aptamers *via* nanostructures is a well-documented effect.[40,41] Nanostructure employment can increase the robustness of the surface which leads to higher stability of surface immobilization.

Conclusions

In this work, the surface nano-dimensionality and the corresponding influence on the E-AB sensor performance were investigated. Two bottom-up approaches, a template-based synthesis using TEPC and electrochemical deposition, were used to build and synthesize 1D gold NRs (ECSA = 0.072 cm^2) and 3D gold NSs (ECSA = 0.079 cm^2), respectively. After attachment of aptamers on the various Au surfaces using gold-thiol chemistry, the analytical performances were measured and compared to the regular gold electrode (ECSA = 0.02 cm^2) as the benchmark of the study. The lowest LOD was obtained for the 1D NR with 3.5 nM *versus* 6.8 nM for the 3D NS featuring electrode, compared to 7.8 nM estimated using the control E-AB sensor. Our data revealed that, contrary to the general perception, increasing the surface area not always leads to a higher gain if there is a morphological counterplay. Also, the data suggested that the surface/orientation of aptamers, on top of the alkanethiols SAM, may strongly rely on the surface morphology features and eventually affects the sensor performance/sensitivity. But the surface enhancement on the electrode due to the application of NS and NR demonstrated a significant improvement in the shelf-life of the E-AB sensors (~9 days) relative to the control sensor with a planar surface (~3 days). Studying various aptamer lengths on the nanoscale surface is required to confirm its effect on sensor performance, including aptamer's surface organization and target-probe dynamics.

Author contributions

Conceptualization, AK and G. M.; methodology, A. K.; validation, AK; formal analysis, AK; resources, G. M.; data curation, AK; writing—original draft preparation, A. K.; writing—review and editing, E. H. and G. M.; supervision, G. M.; funding acquisition, G. M. All authors have read and agreed to the published version of the manuscript.

Conflicts of interest

There are no conflicts to declare.

Acknowledgements

This research was funded by NSERC discovery grant (RGPIN-2020-05884) and FRQS chercheur boursier J1 (266388).

References

1 N. S. Que-Gewirth and B. A. Sullenger, *Gene Ther.*, 2007, **14**, 283–291.
2 S. Song, L. Wang, J. Li, C. Fan and J. Zhao, *TrAC, Trends Anal. Chem.*, 2008, **27**, 108–117.
3 C. M. Dollins, S. Nair and B. A. Sullenger, *Hum. Gene Ther.*, 2008, **19**, 443–450, **https://home.liebertpub.com/hum**.
4 Y. Xiao, R. Y. Lai and K. W. Plaxco, *Nat. Protoc.*, 2007, **2**, 2875–2880.
5 M. Sharafeldin and J. J. Davis, *Anal. Chim. Acta*, 2022, **1216**, 339759.
6 J. Muñoz, R. Montes and M. Baeza, *TrAC, Trends Anal. Chem.*, 2017, **97**, 201–215.
7 D. Bizzotto, I. J. Burgess, T. Doneux, T. Sagara and H. Z. Yu, *ACS Sens.*, 2018, **3**, 5–12.
8 J. J. Gooding and N. Darwish, *Chem. Rec.*, 2012, **12**, 92–105.
9 Y. Xiao, T. Uzawa, R. J. White, D. DeMartini and K. W. Plaxco, *Electroanalysis*, 2009, **21**, 1267–1271.
10 T. Cholko and C. E. A. Chang, *J. Phys. Chem. B*, 2021, **125**, 1746–1754.
11 M. Lin, J. Wang, G. Zhou, J. Wang, N. Wu, J. Lu, J. Gao, X. Chen, J. Shi, X. Zuo and C. Fan, *Angew. Chem.*, 2015, **127**, 2179–2183.
12 A. L. Furst, M. G. Hill and J. K. Barton, *Langmuir*, 2013, **29**, 16141–16149.
13 A. B. Steel, R. L. Levicky, T. M. Herne and M. J. Tarlov, *Biophys. J.*, 2000, **79**, 975–981.
14 T. M. Herne and M. J. Tarlov, *J. Am. Chem. Soc.*, 1997, **119**, 8916–8920.
15 F. Ricci, R. Y. Lai, A. J. Heeger, K. W. Plaxco and J. J. Sumner, *Langmuir*, 2007, **23**, 6827–6834.
16 F. Ricci, N. Zari, F. Caprio, S. Recine, A. Amine, D. Moscone, G. Palleschi and K. W. Plaxco, *Bioelectrochemistry*, 2009, **76**, 208–213.

17 M. D. Mayer and R. Y. Lai, *Talanta*, 2018, **189**, 585–591.
18 C. Y. Lee, P. Gong, G. M. Harbers, D. W. Grainger, D. G. Castner and L. J. Gamble, *Anal. Chem.*, 2006, **78**, 3316–3325.
19 K. K. Leung, A. D. Gaxiola, H. Z. Yu and D. Bizzotto, *Electrochim. Acta*, 2018, **261**, 188–197.
20 N. Dimcheva, *Curr. Opin. Electrochem.*, 2020, **19**, 35–41.
21 K. Urmann, J. Modrejewski, T. Scheper and J. G. Walter, *BioNanoMaterials*, 2016, DOI: **10.1515/BNM-2016-0012**.
22 M. Shariati, M. Ghorbani, P. Sasanpour and A. Karimizefreh, *Anal. Chim. Acta*, 2019, **1048**, 31–41.
23 F. Tulli, F. A. Gulotta, D. M. Martino, V. I. P. Zanini and C. D. Borsarelli, *J. Electrochem. Soc.*, 2018, **165**, B452–B457.
24 N. Kumar and S. Kumbhat, *Essentials in Nanoscience and Nanotechnology*, 2016, pp. 326–360.
25 P. N. Navya and H. K. Daima, *Nano Convergence*, 2016, **3**, 1.
26 P. R. Solanki, A. Kaushik, V. V. Agrawal and B. D. Malhotra, *NPG Asia Mater.*, 2011, **3**, 17–24.
27 Q. Zhou and T. Kim, *Sens. Actuators, B*, 2016, **227**, 504–514.
28 L. Soleymani, Z. Fang, E. H. Sargent and S. O. Kelley, *Nat. Nanotechnol.*, 2009, **4**, 844–848.
29 P. E. Sheehan and L. J. Whitman, *Nano Lett.*, 2005, **5**, 803–807.
30 I. Hammami, N. M. Alabdallah, A. Al Jomaa and M. Kamoun, *J. King Saud Univ., Sci.*, 2021, **33**(7), DOI: **10.1016/J.JKSUS.2021.101560**.
31 Z. Yan, M. G. Taylor, A. Mascareno and G. Mpourmpakis, *Nano Lett.*, 2018, **18**, 2696–2704.
32 M. G. Taylor, N. Austin, C. E. Gounaris and G. Mpourmpakis, *ACS Catal.*, 2015, **5**, 6296–6301.
33 K. M. Bratlie, H. Lee, K. Komvopoulos, P. Yang and G. A. Somorjai, *Nano Lett.*, 2007, **7**, 3097–3101.
34 M. Arenz, U. Landman and U. Heiz, *ChemPhysChem*, 2006, **7**, 1871–1879.
35 X. J. Huang, A. M. O'Mahony and R. G. Compton, *Small*, 2009, **5**, 776–788.
36 A. Walcarius, S. D. Minteer, J. Wang, Y. Lin and A. Merkoçi, *J. Mater. Chem. B*, 2013, **1**, 4878–4908.
37 L. Shi, Z. Chu, X. Dong, W. Jin and E. Dempsey, *Nanoscale*, 2013, **5**, 10219–10225.
38 A. M. Downs, J. Gerson, M. N. Hossain, K. Ploense, M. Pham, H. B. Kraatz, T. Kippin and K. W. Plaxco, *ACS Sens.*, 2021, **6**, 2299–2306.
39 N. Arroyo-Currás, K. Scida, K. L. Ploense, T. E. Kippin and K. W. Plaxco, *Anal. Chem.*, 2017, **89**, 12185–12191.
40 X. Bin, E. H. Sargent and S. O. Kelley, *Anal. Chem.*, 2010, **82**, 5928–5931.
41 S. Ranjbar, S. Shahrokhian and F. Nurmohammadi, *Sens. Actuators, B*, 2018, **255**, 1536–1544.
42 C. S. M. Ferreira, C. S. Matthews and S. Missailidis, *Tumor Biol.*, 2006, **27**, 289–301.
43 B. Plowman, S. J. Ippolito, V. Bansal, Y. M. Sabri, A. P. O'Mullane and S. K. Bhargava, *Chem. Commun.*, 2009, 5039–5041.
44 Q. Cao, Z. Shao, D. K. Hensley, N. V. Lavrik and B. J. Venton, *Langmuir*, 2021, **37**, 2667–2676.
45 D. W. M. Arrigan, *Analyst*, 2004, **129**, 1157–1165.
46 A. A. Lubin and K. W. Plaxco, *Acc. Chem. Res.*, 2010, **43**, 496–505.
47 H. D. Hill, J. E. Millstone, M. J. Banholzer and C. A. Mirkin, *ACS Nano*, 2009, **3**, 418–424.
48 H. D. Hill, J. E. Millstone, M. J. Banholzer and C. A. Mirkin, *ACS Nano*, 2009, **3**, 418–424.
49 A. A. Lubin, B. V. S. Hunt, R. J. White and K. W. Plaxco, *Anal. Chem.*, 2009, **81**, 2150–2158.
50 S. S. Mahshid, S. Camiré, F. Ricci and A. Vallée-Bélisle, *J. Am. Chem. Soc.*, 2015, **137**, 15596–15599.
51 J. N. Miller, J. C. Miller and R. D. Miller, *Statistics for Analytical Chemistry*, Pearson Education, England, 4th edn, 2000, ch. 7, p. 292.